ORIGINAL PAPER

Numerical study of the precipitation diurnal variation and its relationship with cloud radiative heating during the Meiyu period in 2020

Lu Gao[1] · Qian Huang[1] · Suxiang Yao[1] · Tianle Sun[1]

Abstract

Based on hourly rain gauge observation, cloud amount, and radiative fluxes data from the Clouds and the Earth's Radiant Energy System (CERES) and ECMWF Reanalysis v5 (ERA5) dataset, the precipitation process during the Meiyu period in the middle and lower reaches of the Yangtze River in 2020 was simulated in WRF to reveal the influence of cloud radiative heating process on the diurnal variation of precipitation using multiple cloud microphysical schemes. The statistical evaluation of three microphysical parameterization schemes shows that the two-moment scheme WDM6 is more reasonable than the other two schemes in simulating the precipitation distribution, central intensity, and cloud characteristic distribution. There are significant bimodal characteristics in the diurnal variation of precipitation during the Meiyu period by analyzing the observation data. The numerical experiment accurately simulated the time and magnitude of the early morning peak in the heavy rain area but failed to reproduce the peak in the late afternoon, resulting in a false weak rainfall accumulation. The comparison of simulation results with the observed cloud macroscale and microscale characteristics revealed that the reason for the deviation of precipitation simulation was closely related to the inaccurate description of cloud microphysical quantities. The lack of ice phase cloud droplets led to excessively strong radiative heating rate at 200–500 hPa, resulting in anomalous warming in the mid-upper troposphere. Meanwhile, the cold advection at 850 hPa led to anomalous cooling in the lower troposphere, increasing atmospheric stability and further inhibiting the development of the afternoon thermal convection process.

1 Introduction

Meiyu is a climatic phenomenon that occurs every June and July in the middle and lower reaches of the Yangtze River in China, in Taiwan, in south-central Japan, and in southern Korea (Guan et al. 2020; Liu and Ding 2020). The frequent heavy precipitation during the Meiyu period often brings serious flooding to the middle and lower reaches of the Yangtze River in China (Huang et al. 2006; Ding et al. 2007; Liu and Ding 2020). Improving the prediction accuracy of

the precipitation cycle in the Meiyu period has always been an important and difficult subject in the meteorological administration and scientific research area.

Precipitation in the Meiyu period has complex diurnal variation characteristics (Yu et al. 2007a, b; Chen et al. 2012, 2013; Xue et al. 2018; Zhang et al. 2020a, b). Unlike the midnight peak of precipitation in southwest China and the early-morning peak of precipitation in the upper reaches of the Yangtze River (Xu and Zipser 2015; Jiang et al. 2017), the Meiyu area has double peak' morphological characteristics that appear in the morning and afternoon, respectively (Li et al. 2008, 2010; Zhou et al. 2008; Yin et al. 2009; Wang et al. 2011; Yuan et al. 2012; Yu et al. 2014a, b; Yu and Li 2016). Mu et al. (2021) believed that the precipitation peak in the early morning of summer in Eastern China is mainly caused by the synoptic scale persistent precipitation process, while the peak in the afternoon is composed of short-term convective precipitation. Chen et al. (2020) compared the bimodal distribution characteristics of precipitation in the middle and lower reaches of the Yangtze River from June to

Responsible Editor: Clemens Simmer, Ph.D.

✉ Qian Huang
huangq@nuist.edu.cn

1 Key Laboratory of Meteorological Disaster (KLME), Ministry of Education & Collaborative Innovation Center On Forecast and Evaluation of Meteorological Disasters (CIC-FEMD), Nanjing University of Information Science & Technology, Nanjing, China

July 2020. The early morning peak intensity is significantly stronger than the afternoon peak intensity, and the latter is closely related to the local buoyancy convection process driven by the diurnal variation of solar radiation (Zeng et al. 2022).

With the increasing requirement for refined precipitation forecast system, the inversion of the precipitation diurnal variation by the numerical model has attracted more and more attention. The diurnal variation of precipitation simulated by general circulation models generally has common deficiencies like earlier afternoon peak, the stronger amplitude of diurnal variation, and less significant night rain (Kendon et al. 2012; Zhong et al. 2022), which are related to the insufficient description of the subgrid convection process (Huang et al. 2011; Yuan 2013). There is also great uncertainty in the simulation of diurnal variation of precipitation by high resolution regional model and mesoscale model (Yu et al. 2014a, b). The preliminary study confirmed that increasing the model resolution alone cannot effectively improve the simulation; the key to improvement is to reduce the uncertainty in the parameterization scheme of cloud-precipitation processes (Yuan et al. 2013). When the mesoscale meteorological model is used to carry out high-resolution numerical simulation, the simulation of clear sky radiation flux is generally satisfactory. However, in cloudy and rainy weather, the simulated cloud radiative forcing often tends to deviate greatly from the gauge observations (Shen and Hu 2006; Wen et al. 2010; Wang et al. 2012; Zhou et al. 2020). Most of the uncertainties found in the numerical simulation of multi-scale variability of precipitation in East Asia are related to cloud radiation and its feedback process (Zhang et al. 2017; Medeiros et al. 2021).

There are many research conclusions on the physical mechanisms of cloud-induced radiation processes affecting precipitation by altering the atmospheric vertical stability (Ackerman et al. 1988; Christensen et al. 2013; Harrop and Hartmann 2016; Zhang et al. 2017). Clouds can enhance the planetary albedo by reflecting solar radiation to space to cool the Earth, and trapping outgoing long-wave infrared radiative flux to warm the Earth, thus significantly affecting the vertical temperature profile and atmospheric circulation (Yu et al. 2004; Kato et al. 2008; Wu et al. 2023). Therefore, there are both direct and indirect physical connections between the generation and disappearance of clouds and regional precipitation (Lin et al. 2000; Zhang et al. 2017; Wu and Chen 2021). More assessment studies have pointed out that the inversion of the model for cloud macro- and micro-characteristics greatly affects the accuracy of the simulating cloud radiation effect, leading to varying degrees of deviation in simulated precipitation (Wang and Ding 2005; Yin and Porporato 2017; Varga and Breuer 2020). Zhou et al. (2005) revealed that the interaction between clouds and radiation modified atmospheric dynamic conditions through the radiation-convection trigger mechanism, which in turn caused changes in the convection and ultimately enhanced or weakened precipitation on the ground.

From June to July 2020, the persistent and widespread heavy precipitation process in the Yangtze-Huaihe basin was typically extreme and caused severe flooding and geological disasters (Liu and Ding 2020; Zhang et al. 2020a, b), while most numerical weather forecast products had large deviations in terms of precipitation area and diurnal variation (Cai et al. 2020; Chen et al. 2020; Jiao et al. 2021; Bu et al. 2022). So what are the main reasons for these forecast model deviations? Is it related to cloud radiation processes? To answer these questions, gauge observations and reanalysis data combined with a high-resolution WRF model were used to simulate and evaluate the precipitation process during the 2020 Meiyu period. On this basis, the model results were used to systematically analyze the diurnal variation characteristics of precipitation in the study area and discuss the influence of cloud radiation processes on the diurnal bias of simulated precipitation, with a view to revealing the root causes of model simulation deviations, identifying entry points for model improvement, and providing scientific support for the fine assessment and correction of numerical models.

2 Data and methodology

2.1 Data

Cloud fraction and radiative flux data are provided by the latest SYN1deg-Ed4.1A dataset from Clouds and the Earth's Radiant Energy System (CERES) (https://ceres.larc.nasa.gov/data/). As one of the three major CERES product sets, the Synoptic Radiative Fluxes and Clouds (SYN) dataset is provided continuous global all-sky observations with hourly resolution and $1° \times 1°$ resolution via geostationary satellites (GEO) and is suitable for local diurnal process studies (Doelling et al. 2016). This dataset contains radiative fluxes from the top of atmosphere (TOA), the ground, and four atmospheric pressure levels (70 hPa, 200 hPa, 500 hPa, and 850 hPa) in the vertical direction, as well as cloud properties from MODIS and GEO at different altitudes (high, medium–high, medium–low, low), including cloud fraction, particle radius, optical thickness, top height, etc (CERES_SYN1deg_Ed4A Data Quality Summary, 2021). (https://ceres.larc.nasa.gov/documents/DQ_summaries/CERES_SYN1deg_Ed4A_DQS.pdf, accessed on 13 December 2021).

The observed precipitation data used in this article is a high spatiotemporal gauge-satellite merged hourly, $0.1° \times 0.1°$ precipitation dataset from the China Meteorological Administrator (CMA), using hourly rain gauge data at more than 30,000 automatic weather stations in China in

conjunction with the Climate Precipitation Center Morphing (CMORPH) precipitation product (http://data.cma.cn/site/index.html). It has been widely used for the study of extreme weather events (Shen et al. 2013). To verify the accuracy of this merged precipitation product, we compared it with the daily gauge-based precipitation from 2479 manned national meteorological observation stations in China.

The fifth-generation global atmospheric reanalysis data (ERA5) from the European Centre for Medium-Range Weather Forecasts (ECMWF) was used to analyze the circulation characteristics, including specific humidity, temperature, geopotential height, and wind velocity, with a horizontal resolution of $0.25° \times 0.25°$ and a temporal interval of 1 h and 37 layers in the vertical direction (Hersbach et al. 2020) (https://cds.climate.copernicus.eu/cdsapp#!/dataset/reanalysis-era5-pressure-levels?tab=overview). ERA5 reanalysis data on hourly high temporal resolution provides more detailed information on the evolution of extremely heavy precipitation (Dee et al. 2011; Hersbach et al. 2020). In addition, the ERA5 data adopt a more complete parameterization scheme for the clouds-involved precipitation process, which is improved from the original two fore-cast quantities of cloud water and cloud cover fraction to five forecast quantities of cloud liquid water, cloud ice, rain water, snow, and cloud cover fraction, which can reproduce the generation and

extinction processes of clouds and precipitation more realistically, and to a certain extent can be used as a substitute for the observations to test the numerical model simulation results (Hersbach et al. 2020).

2.2 Model and experimental design

In this study, WRF V4.3 was used to perform 84 consecutive hours of simulation every day from May 31 to July 31, 2020. We selected 12:00 a.m. (UTC) as the model start time for each case, where the first 12 h's simulation result was discarded as the spin-up time for the cold start (Fig. 1a). Therefore, a total of 61 individual cases were carried out using this sliding simulation method, each containing 72 h of valid simulation results. The experiments used three resolutions of 27 km, 9 km, and 3 km nested coupling, and the simulation area is shown in Fig. 1b. The initial and boundary conditions for the WRF model simulation were obtained from the National Centers for Environmental Prediction (NCEP) $1° \times 1°$ Final Analysis (FNL) dataset. Details model setting and the main physical parameterizations are listed in Table 1. In this study, we used three cloud microphysics schemes of WSM3, WSM6, and WDM6 (Hong et al. 2004; Hong and Lim 2006; Lim and Hong 2010) at domains D01, D02, and D03, and the
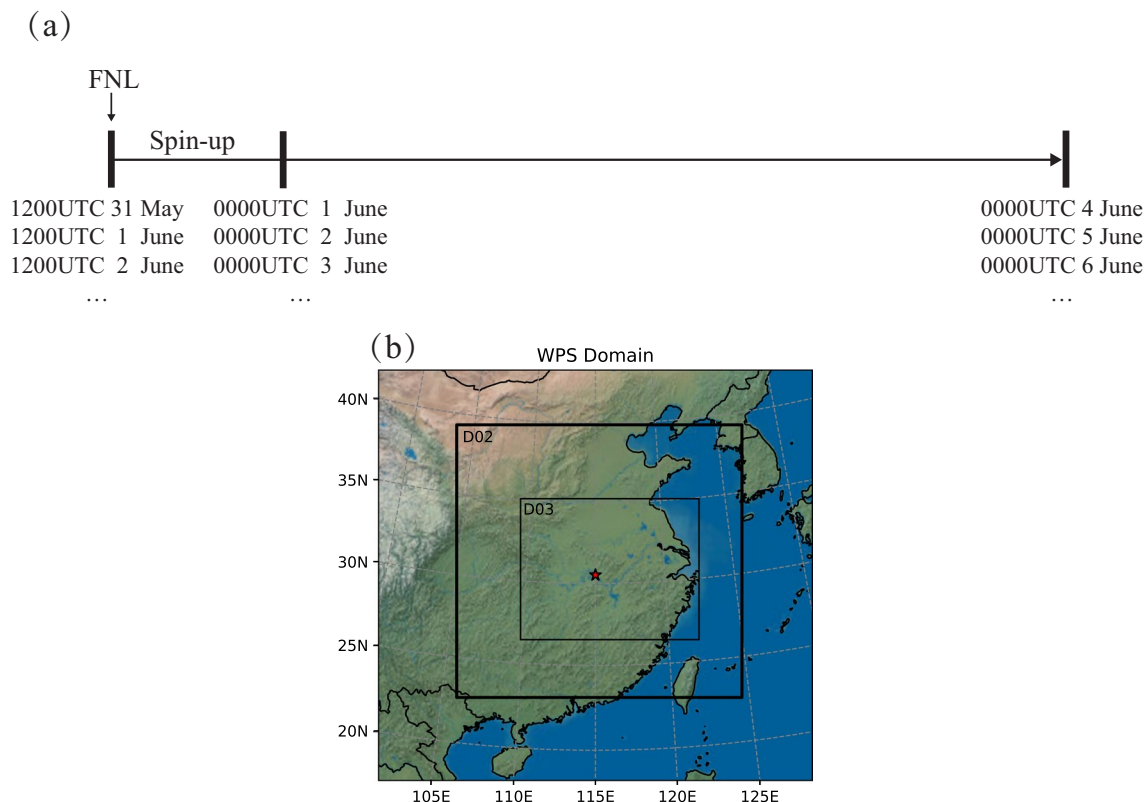

Fig. 1 **a** Time scheme of experiment. **b** Nested simulation domains of the WRF model

Table 1 Description of the model settings

Domain	D01	D02	D03	References
Horizontal grids	112×105	220×208	412×322	/
Resolution	27 km	9 km	3 km	/
Time step (s)	90 s	30 s	10 s	/
SW radiation	RRTMG	RRTMG	RRTMG	Iacono et al. (2008)
LW radiation	RRTMG	RRTMG	RRTMG	Iacono et al. (2008)
PBL	YSU	YSU	YSU	Hong et al. (2006)
Cumulus	Kain-Fritsch	Kain-Fritsch	/	Kain (2004)
Microphysics	WSM3	WSM3	WSM3	Hong et al. (2004)
	WSM6	WSM6	WSM6	Hong and Lim (2006)
	WDM6	WDM6	WDM6	Lim and Hong (2010)
Land surface	Noah	Noah	Noah	Niu et al. (2011)

Table 2 Contingency table of prediction results and observations for a selected precipitation threshold

Observation	Predictions	
	Yes	No
Yes	NA	NC
No	NB	ND

cumulus parameterization scheme of Kain Fritsch (Kain 2004) only at domain D01 and D02.

2.3 Assessment method

In this study, we evaluated the simulations for precipitation and cloud cover fraction during the Meiyu period by calculating the spatial and time correlation coefficient, mean error (ME), root mean square error (RMSE), correlation coefficient (CC) and threat score (TS). The formulas for their calculations are as follows:

$$\text{ME} = \bar{p} - \bar{o} \tag{1}$$

$$\text{RMSE} = \sqrt{\frac{1}{N} \sum_{i=1}^{N} \left(p_i - o_i\right)^2} \tag{2}$$

$$CC = \frac{\frac{1}{N-1}\left[\sum_{i=1}^{N}\left[(p_i-\bar{p})(o_i-\bar{o})\right]\right]}{\left[\frac{1}{N-1}\left[\sum_{i=1}^{N}(p_i-\bar{p})^2\right]\right]^{\frac{1}{2}}\left[\frac{1}{N-1}\left[\sum_{i=1}^{N}(o_i-\bar{o})^2\right]\right]^{\frac{1}{2}}} \tag{3}$$

$$TS = \frac{NA}{NA+NB+NC} \tag{4}$$

where N is the total number of observed or predicted precipitation data, p_i and o_i are the predicted and observed data, respectively. The $\bar{p}$ and $\bar{o}$ are the average value predicted and observed data, respectively. The description of NA, NB, and NC is indicated in Table 2.

All model outputs are interpolated to the same spatial resolution as the observed data before analysis, where the precipitation is $0.1° \times 0.1°$ and the cloud features are $1° \times 1°$.

2.4 Total cloud cover

The fraction cloud cover is calculated following the semi-empirical cloudiness parameterization developed by Xu and Randall on each level (Xu and Randall 1996). To compare with the observation, it is necessary to apply an overlap assumption scheme to convert the cloud fraction at each model level to total cloud cover. The vertical superposition scheme of clouds selected in this paper adopted the maxi-mum-average overlap scheme, that is, the vertical average cloud fraction of non-adjacent two-layer cloud fraction separated by the clear sky is first calculated, and then the maximum value of the average cloud fraction of different cloud blocks in the vertical direction is selected as the total cloud cover (Zheng et al. 2013).

2.5 Definition of cloud radiation heating rate

Radiation heating rate is a non-adiabatic heating change caused by the vertical gradient difference of net radiation flux. The calculation of the radiative heating rate (Cesana et al. 2019) is shown below:

$$F_{net}(z) = F^{\uparrow}(z) + F^{\downarrow}(z) \tag{5}$$

$$\Delta F_{net} = F_{net}(z + \Delta z) - F_{net}(z) \tag{6}$$

$$HR = \left(\frac{dT}{dt}\right) = -\frac{1}{\rho c_p}\frac{dF_{net}}{dz} = \frac{g}{c_p}\frac{dF_{net}}{dp}, \quad \left(g = 9.81, c_p = 1004\right) \tag{7}$$

where F is the radiation flux (W m^{-2}), F_{net} is the net radiation flux (W m^{-2}), HR is the radiation heating rate (K h^{-1}), T is the temperature (K), t is time (h), g is the acceleration due to gravity (m s^{-2}), ρ is the air density (kg m^{-3}), c_p is the specific heat content of air at constant pressure (J kg^{-1} K^{-1}), and p is the pressure (Pa). The z and $z + \Delta z$ indicate the lower and upper boundary of the layer, respectively. The subscripts ↑ and ↓ indicate the upward radiation flux and the downward radiation flux, respectively.

In this paper, the cloud radiative heating rate is defined as the difference between the radiative heating rate under all-sky and clear-sky conditions, which can be used to estimate the influence of clouds on radiative heating in the atmosphere (Cesana et al. 2019).

3 Results

3.1 Simulation assessment of precipitation during the 2020 Meiyu period

First, the spatial distribution of accumulated precipitation in the middle and low region of the Yangtze River between June 1 and July 31, 2020, during the Meiyu period was compared between gauge observation (Fig. 2a) and merged precipitation product (Fig. 2b). It can be seen from the figures that the precipitation in Meiyu period is mainly concentrated near 28°–32°N, with two precipitation extreme centers over
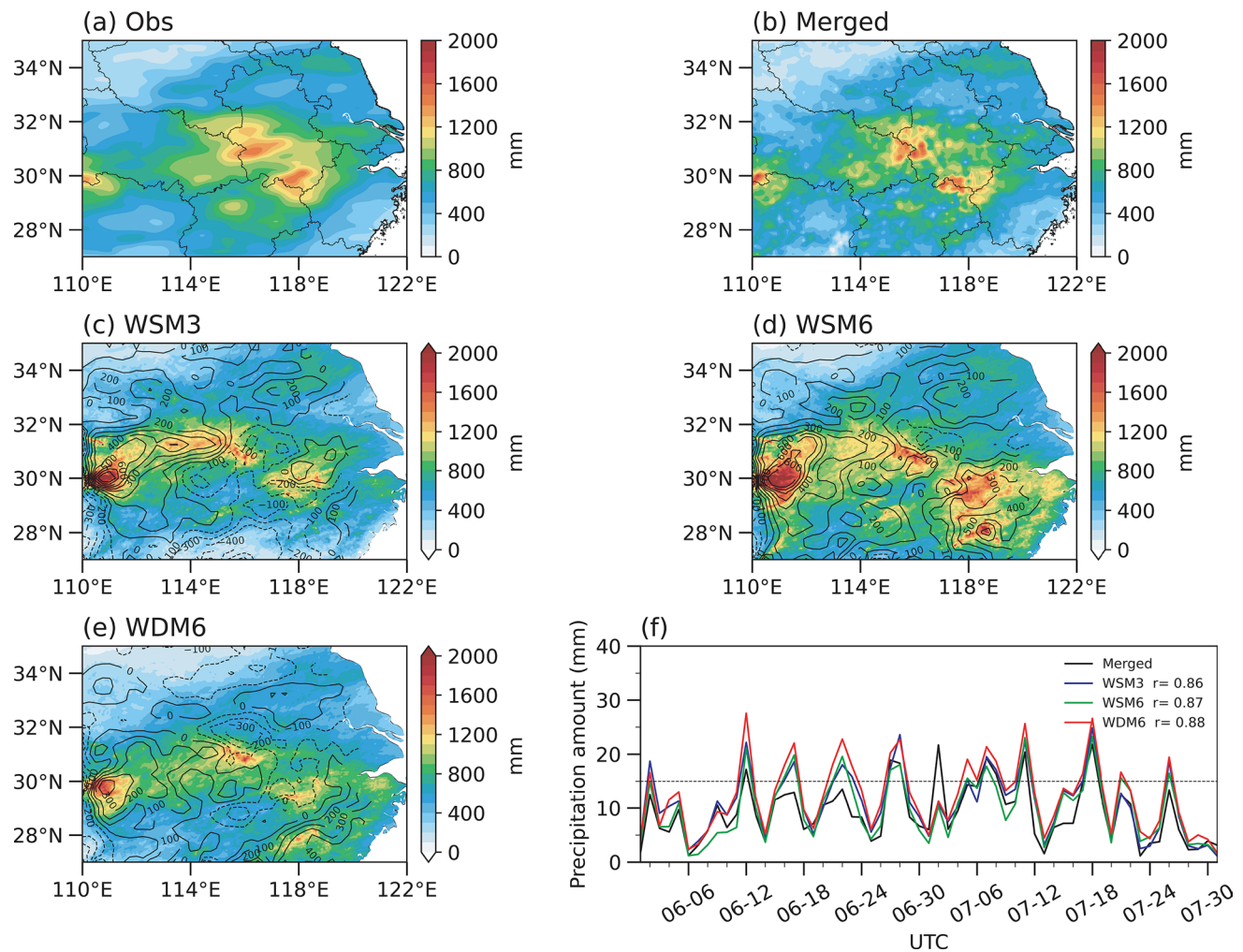
Fig. 2 Distribution of accumulated precipitation (shaded; units: mm) of observational data of stations (**a**), merged precipitation product (**b**) and WSM3 scheme (**c**) WSM6 scheme (**d**), WDM6 scheme (**e**) simulated from June to July 2020. The contours show the bias of the simulation (simulation minus observation, the same as below). **f** The regional average daily evolution precipitation in the middle and lower reaches of the Yangtze River (110°–122° E, 27°–35° N) from June to July 2020. Daily precipitation of 15 mm/d is indicated by the horizontal dashed line

1200 mm. The precipitation and its distribution revealed by the merged precipitation product data are well consistent with the gauge observation. Comparing the numerical simulation results (Fig. 2c–e), it is found that the simulated precipitation distribution of the three schemes is close to the observations, but the precipitation in the west and southeast of the main rain area is underestimated to varying degrees, and the WDM6 scheme has the best performance. By comparing the regional average daily precipitation, it is found that the actual and WSM3, WSM6, and WDM6 schemes are 9.12, 10.88, 12.22, and 9.86 mm/day, respectively. The three schemes have a certain overestimation of the average daily precipitation, but the WDM6 scheme has the smallest deviation from the observation. As for the daily evolution

of precipitation (Fig. 2f), it can be found that all three cloud microphysics schemes can well simulate the evolution character. Among them, the WDM6 scheme has the highest time correlation coefficient of 0.88 and the smallest deviation for observation.

The spatial distribution of total cloud fraction between observations and model simulations was further compared. The observation results show that the cloud fraction is less in the north and higher in the southeast of the area (Fig. 3a). The cloud fraction simulated by the three schemes has a certain error compared with the observation (Fig. 3b–d), the underestimation is from 5 to 15%, and the spatial correlation coefficients are as low as about 0.4, which cannot present the high-value center in the southeast.

Fig. 3 Distribution of hourly average total cloud fraction (shaded) of satellite observation (**a**), and WSM3 scheme (**b**), WSM6 scheme (**c**), WDM6 scheme (**d**) simulated from June to July 2020. The contours indicate the bias of the simulation. The values indicate spatial correlation coefficients
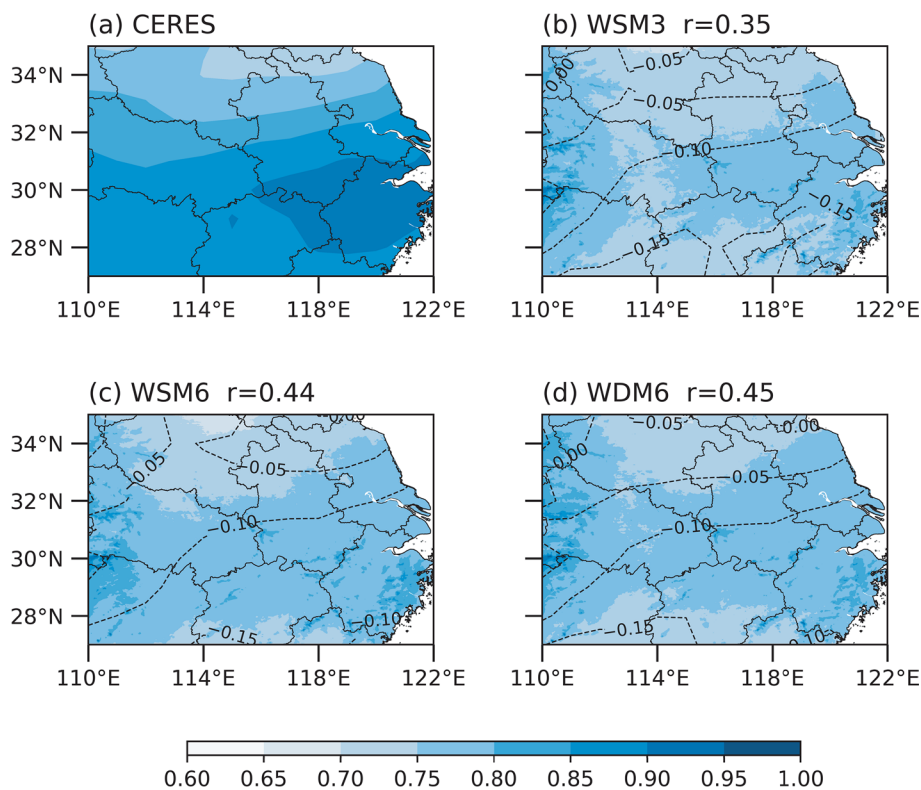
Fig. 4 Diurnal variations of regional average (110°–122° E, 27°–35° N) precipitation (units: mm) (**a**) and CAPE (units: J/kg) (**b**) in June–July 2020. The black line indicates the merged precipitation product, the blue line indicates the WSM3 scheme simulation, the green line indicates the WSM6 scheme simulation, and the red line indicates the WDM6 scheme simulation
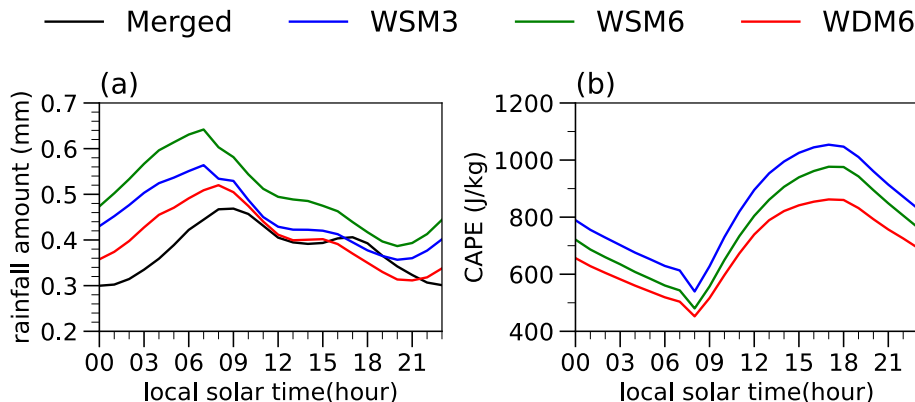
The diurnal variation characteristics of regional average precipitation in the middle and lower reaches of the Yangtze River and the simulation results of different microphysical schemes are analyzed in Fig. 4a. The diurnal variation curve of precipitation in the actual situation is double-peak distribution, with an obvious early morning peak around 07:00–09:00 LST and an afternoon peak around 16:00–17:00 LST. The intensity of the early morning peak is significantly stronger than that of the afternoon precipitation, and the valley value appears at 00:00 LST. All three schemes can well reproduce the early morning peak, and the simulated rainfall intensity is slightly stronger. The occurrence time of the early morning peak in the WSM3 and WSM6 schemes is 2 h earlier than the observation, while the occurrence time of the early morning peak in the WDM6 scheme is consistent with the observation. The afternoon precipitation peak time simulated by the three schemes is ahead of the observation. The WSM3 and WSM6 schemes simulate more afternoon precipitation, while the WDM6 scheme simulated a weaker afternoon peak. The diurnal variation of Convective Available Potential Energy (CAPE) simulated by the three schemes shows a clear single-peaked distribution (Fig. 4b), and the highest CAPE value is reached around 17:00 LST. The simulated CAPE of the WDM6 scheme is somewhat weaker than lower than the other two schemes.

The statistical evaluation of the deviation between the simulation results and the observation (Fig. 5a) shows that the hourly precipitation rate simulated by the WSM6 scheme is generally strong, while the simulated precipitation of the WSM3 and WDM6 schemes shows a positive deviation from night to morning, and turns negative around 18:00 LST.

By comparing the similarity coefficients between simulated and observed daily precipitation changes (Fig. 5c), it is found that the three schemes have obviously lower values at 18:00–21:00 LST, indicating that the model's ability to simulate afternoon precipitation is generally insufficient. Although the TS scores of the three schemes are close (Fig. 5b), the WDM6 scheme has the smallest RMSE in simulating the diurnal variation of precipitation (Fig. 5d).

In summary, the WDM6 scheme can better simulate the precipitation and diurnal variation of precipitation in this Meiyu period, and the simulation results are more reasonable and have better consistency with observation. Huang and Qian (2021) also found that the WDM6 scheme is relatively better than others by evaluating 16 cloud microphysical schemes for a heavy precipitation process in the Yangtze-Huaihe River Basin. Therefore, we selected the simulation results of the WDM6 scheme to further explore the influence mechanism of the cloud radiation process on the diurnal variation bias of precipitation.

Fig. 5 Mean error (ME) (**a**), threat score (TS) (**b**), correlation coefficient (CC) (**c**), and root mean square error (RMSE) (**d**) of the diurnal variations of simulated and observation for the regional average (110°–122° E, 27°–35° N) for June–July 2020. The blue line indicates the WSM3 scheme simulation, the green line indicates the WSM6 scheme simulation and the red line indicates the WDM6 scheme simulation
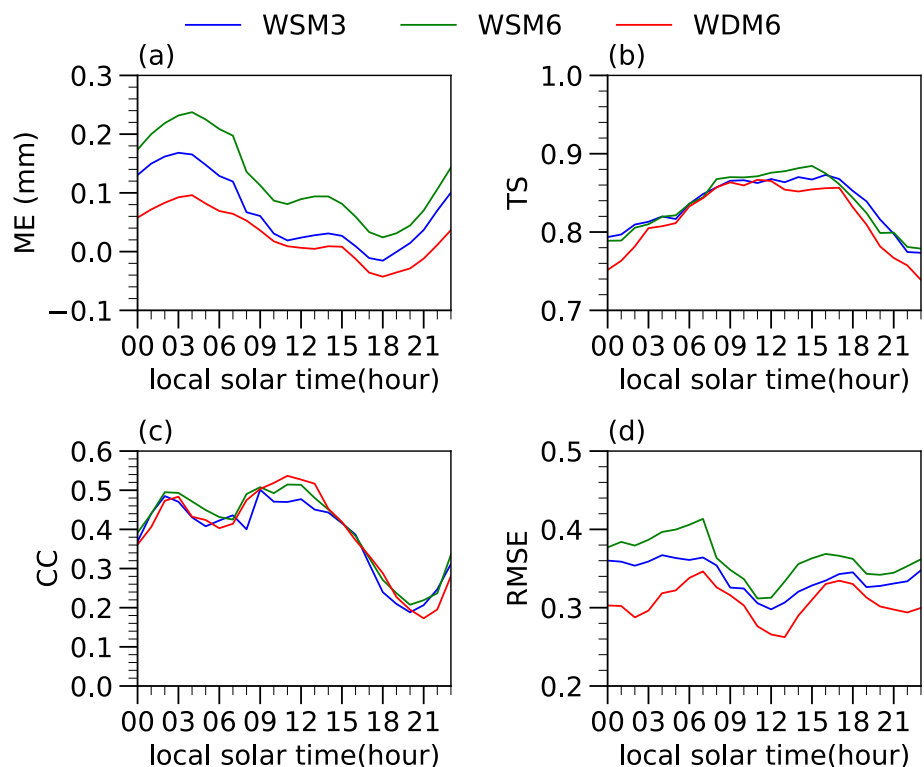
Fig. 6 Time-latitude cross section of precipitation (shaded; units: mm) averaged over 115°–119° E (**a**) and time-longitude cross section of precipitation averaged over 29°–32° N (**b**) in June–July 2020. The contours indicate the bias of the simulation. (**c**) Diurnal variation of averaged precipitation (unit: mm) of 115°–119° E, 29°–32° N from June to July 2020. The black line shows the observation, and the red line is the WDM6 scheme simulation. The histogram indicates the bias of the simulation, where black represents underestimation and red represents overestimation
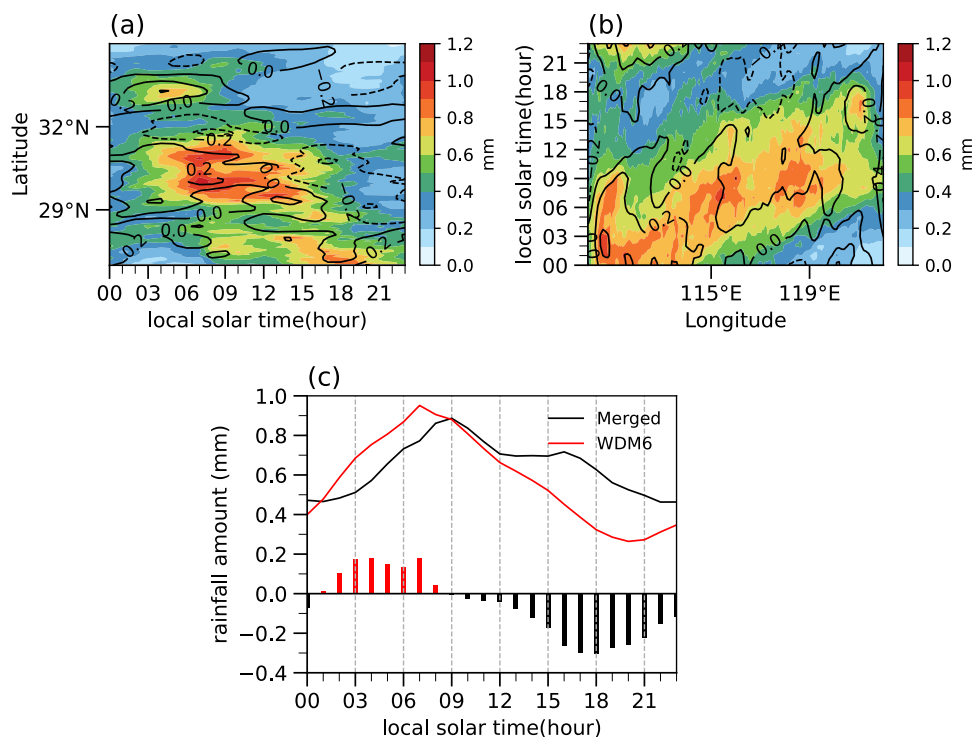
3.2 The relationship between simulation deviation of diurnal variation of precipitation and cloud radiation

Firstly, the diurnal variation characteristics of the precipitation extreme center during the Meiyu period and the bias of simulation were analyzed. Figure 6a shows the time-latitude cross-section of precipitation averaged over 115°–119° E. It can be found that in the range of 29°–32° N, there is some positive deviation in the simulated precipitation at 00:00–09:00 LST and a large negative deviation at 15:00–21:00 LST. Further comparison of the diurnal variation and regional mean precipitation (115°–119° E, 29°–32° N) (Fig. 6c) shows that the double-peak feature is described above. In contrast, the WDM6 scheme simulates the diurnal variation in the precipitation central region as a single-peak distribution, the simulation overestimates the precipitation at 00:00–09:00 LST, fails to reproduce the peak of precipitation in the afternoon, and has a significant negative deviation for the simulation of precipitation from 15:00 to 21:00 LST.

Like precipitation, cloud fraction also has clear diurnal variation characteristics which vary with the type of cloud (Chen and Wang 2016). Ge et al. (2021) found that the transformation of the phase of the cloud's diurnal variation might significantly affect the diurnal variation of precipitation. Therefore, the whole model layers were interpolated and rebuilt to four layers of lower than 700 hPa(low), 700–500 hPa(mid-low), 500–300 hPa (mid-high), and

higher than 300 hPa (high), and the simulated cloud fraction for each layer was averaged and compared to CERES product (Fig. 7a–d). The model can well reproduce the single-peak distribution of low and mid-low cloud cover and the simulation deviation is small. However, there is a large deviation in the simulation of mid-high and high cloud cover, which is concentrated in the period from afternoon to night. In particular, the negative deviations of the simulation at 15:00–02:00 LST are all greater than 0.1 for high cloud fraction. Does the underestimation of afternoon precipitation by the numerical model relate to the bias of cloud simulation?

The distribution of the macro and micro physical characteristics of clouds can affect the vertical stability of the atmosphere by affecting the radiation budget and changing the thermal state of the atmosphere. Therefore, it is necessary to further analyze the vertical velocity, water vapor, and temperature profiles. Figure 8a shows the difference in water vapor mixing ratio and vertical velocity between simulated and observation, and it can be seen that after 12:00 LST, there is a significant anomalous sinking motion, with the maximum deviation occurring from 15:00 to 18:00 LST. Similarly, the simulated water vapor mixing in the 800–600 hPa height range is lower than the observation at 18:00–21:00 LST.

The magnitude of atmospheric vertical stability can significantly affect the development of thermal convection. Simulated deviation profiles of the average temperature at 00:00–09:00 LST and 12:00–21:00 LST are given in Fig. 8b.

Fig. 7 Diurnal variation of averaged low (**a**), mid-low (**b**), mid-high (**c**) and high (**d**) cloud fraction of 115°–119° E, 29°–32° N from June to July 2020. The black line shows the observation, and the blue line is the WDM6 scheme simulation. The histogram indicates the bias of the simulation, where black represents underestimation and red represents overestimation
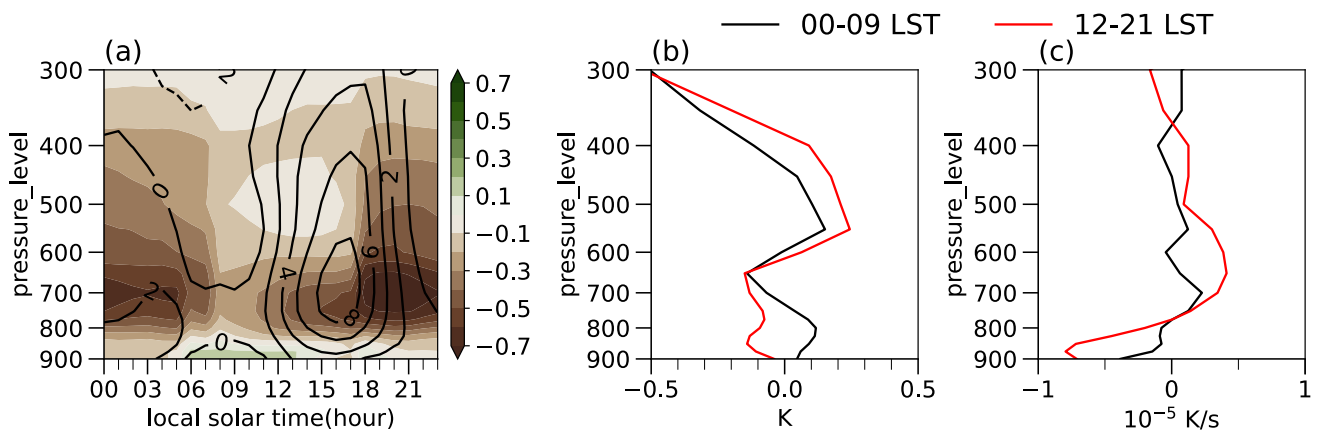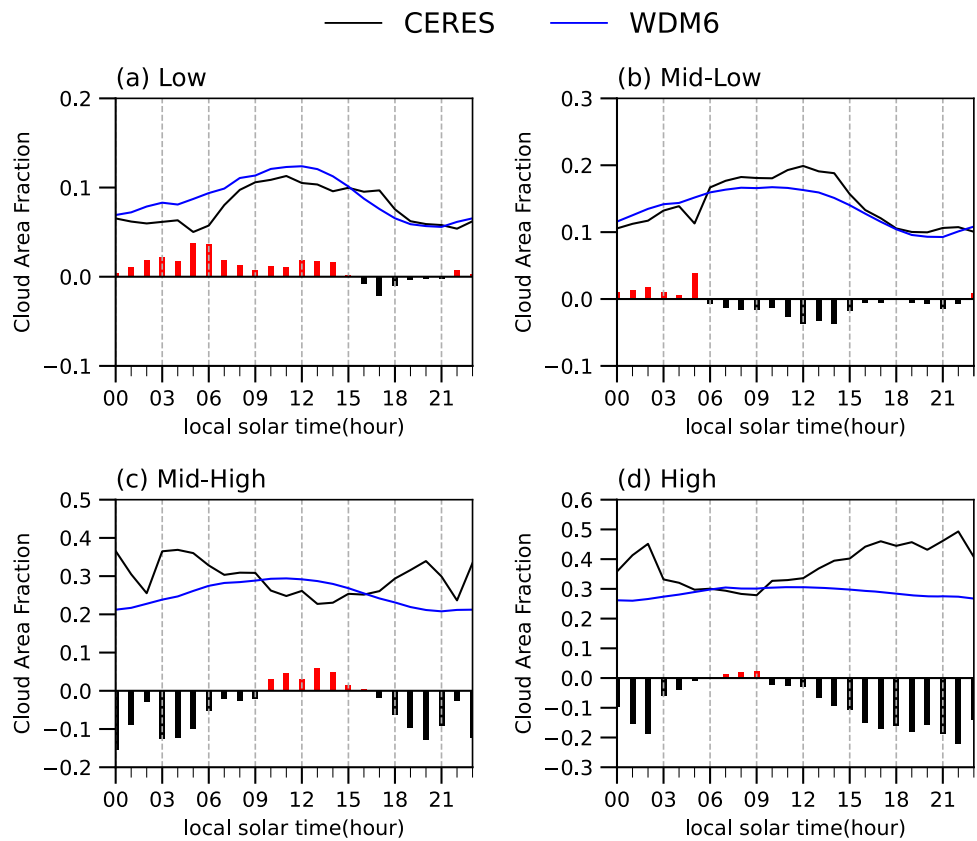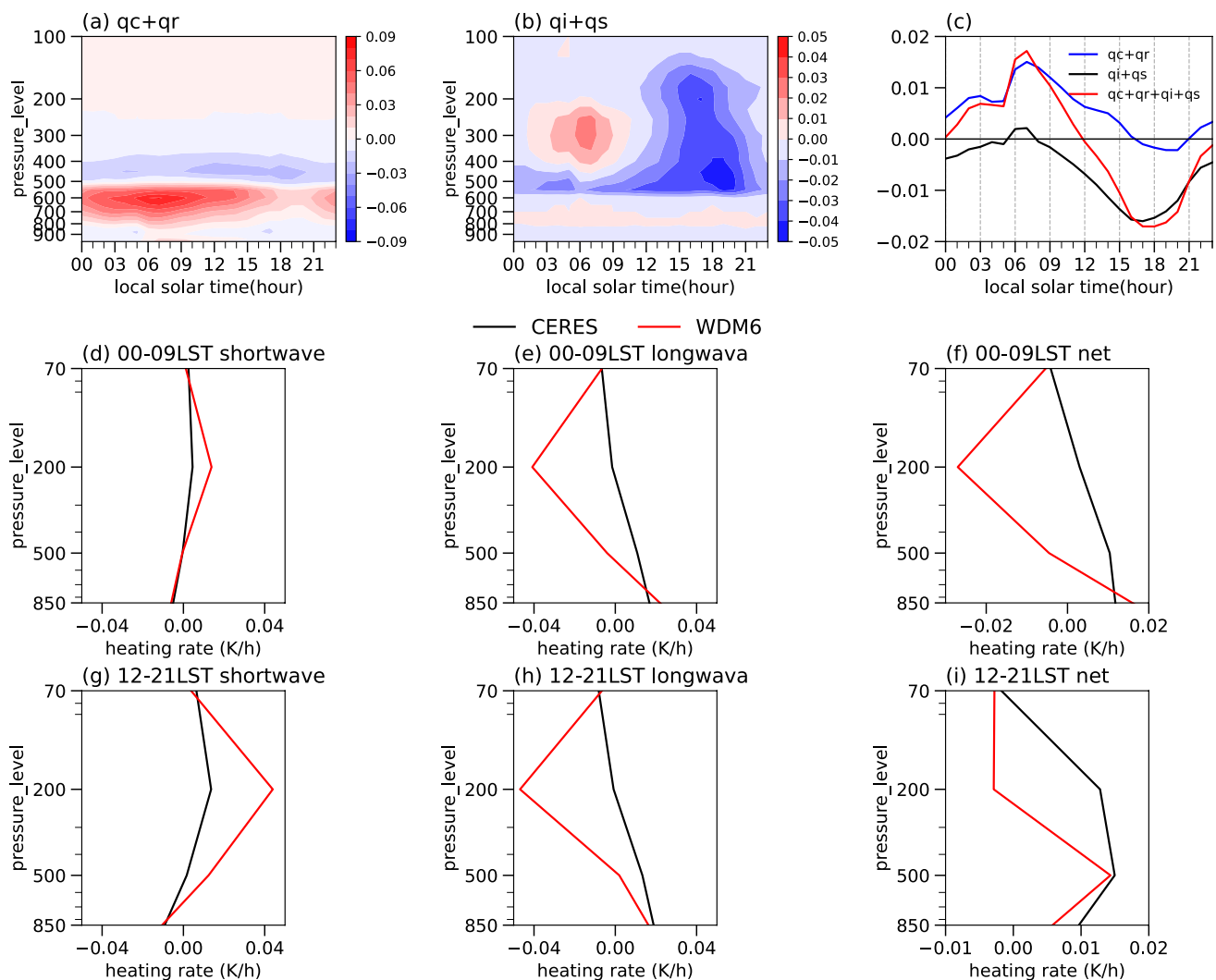

Fig. 8 a Diurnal deviation of averaged water vapor mixing ratio (shaded; units: g/kg) and vertical velocity (contours; units: 0.01 Pa/s) of 115°–119° E, 29°–32° N from June to July 2020. Mean tempera-ture (units: K) deviation profiles (**b**) and temperature advection (units: 10^{-5} K/s) deviation profiles (**c**) from 0000 to 0900 LST (black line) and 1200–2100 LST (red line)

Between 00:00 and 09:00 LST, the temperature of 850 hPa and 500 hPa is consistent with the observation, and between 12:00 and 21:00 LST, the 850 hPa simulation of the lower troposphere is cold, while the 500 hPa of the middle layer turn to abnormally warm. It indicates that the atmosphere below 500 hPa is anomalously stable at 12:00–21:00 LST, inhibiting the development of convection and weakening vertical velocities, eventually discouraging precipitation.

In order to explore the reason why the simulated vertical lapse rate of atmospheric temperature is small, the simulated deviation profiles of the mean temperature advection at 00:00–09:00 LST and 12:00–21:00 LST were further analyzed (Fig. 8c). It can be seen that the simulated temperature advection around 850 hPa at 12:00–21:00 LST is colder than the real situation, resulting in a negative temperature deviation in the lower troposphere at 12:00–21:00 LST. Simulated

Fig. 9 Diurnal deviation of averaged liquid phase hydrometeors (cloud water(qc) and rain water(qr)) mixing ratio (unit: g/kg) (**a**), ice phase hydrometeors (ice(qi) and snow(qs)) mixing ratio (unit: g/kg) (**b**) and total hydrometeors mixing ratio (units: g/kg) (**c**) of 115°–119° E, 29°–32° N from June to July 2020. Average simulated and observed cloud shortwave radiative heating rate (**d, g**), cloud longwave radiative heating rate (**e, h**), and cloud net radiative heating rate (**f, i**) at 0000–0900 LST (**d–f**) and 1200–2100 LST(**g–i**) (unit: K/h)

temperature advection around 500 hPa is not significantly different from the real situation, indicating that the higher simulated temperature in the mid-upper troposphere is not induced by temperature advection.

The change in the heating rate leads to the change in the energy balance of the earth-atmosphere system. The existence of clouds indirectly affects the atmospheric energy balance of each layer by affecting the radiation heating rate. Cloud microphysical characteristics have an important influence on cloud radiative forcing. Different hydrometeors particles also vary considerably in their radiative properties due to differences in optical properties (Wang and Ding 2005; Ge et al. 2021). Figure 9a shows the distribution of the modeled deviation in the vertical direction of regional mean liquid phase hydrometeors (cloud water, rain water)

mixing ratio with time. In the height range of 600–700 hPa, there is a positive deviation extreme value in the simulation at 03:00–09:00 LST, and the deviation gradually decreases until 15:00 LST, and the deviation increases again at night. Figure 9b shows the evolution of the modeled deviation in the vertical direction of the regional mean ice phase hydrometeors (cloud ice and snow) mixing ratio with time. It can be seen that the modeling overestimates the ice phase hydrometeors mixing ratio from 03:00 to 09:00 LST and underestimates it from 15:00 to 21:00 LST, and the deviations are mainly concentrated above 600 hPa. An analysis of the difference between simulated and observed bulk hydrometeors (Fig. 9c) shows that an overestimation of liquid phase hydrometeors mixing ratio leads to redundant bulk hydrometeors mixing ratio at 00:00–12:00 LST, and an underestimation

of the ice phase hydrometeors mixing ratio leads to smaller total hydrometeors mixing ratio at 12:00–23:00 LST.

Further analysis of the influence of clouds on the atmospheric radiative heating rate shows that both the simulation and observed shortwave radiative heating rate (Fig. 9d, g) are positive above the middle troposphere, while the radiative cooling effect is shown below the middle troposphere. The opposite tendency is clear for longwave radiative heating rates (Fig. 9e, h). Comparing the simulated and observed cloud radiative heating rates at 00:00–09:00 LST, it is found that the simulation underestimates the cloud longwave radiative heating rate in the mid-upper troposphere, resulting in an increase in the slope of the net radiative heating rate from 500 to 850 hPa (Fig. 9f). Comparing the simulated and observed cloud radiative heating rates at 12:00–21:00 LST, it is found that the simulation overestimates the cloud shortwave radiative heating rate in the mid-upper troposphere, resulting in a reduction in the slope of the net radiative heating rate from 500 to 850 hPa (Fig. 9i).

In summary, the model simulates a large positive bias in the mixing ratio of liquid phase hydrometeors at 00:00–09:00 LST, resulting in less absorption and scattering of longwave radiation by the atmosphere in the upper troposphere, reducing radiative heating and enhancing the atmospheric temperature lapse rate, which encourages the development of convection and precipitation process at 00:00–09:00 LST. The model simulates a large negative bias in the mixing ratio of ice phase hydrometeors at 15:00–21:00 LST, resulting in more absorption and scattering of shortwave radiation by the atmosphere in the upper troposphere, enhancing radiative heating and reducing the atmospheric temperature lapse rate, which is detrimental to the development of convection and precipitation process, ultimately leading to a large negative bias in the simulation of afternoon precipitation peak.

4 Discussion

The diurnal variation characteristics of precipitation during the Meiyu period and its relationship with cloud radiation were analyzed by using multi-source observation data and a numerical model. It is confirmed that the main reason for the deviation of precipitation simulation is the insufficient description ability of the two-moment cloud microphysical parameterization scheme WDM6 to cloud macro and micro physical characteristics, but how to optimize the parameterization scheme still needs more work to achieve.

5 Conclusions

The WRF model was used to simulate and evaluate the precipitation process during the Meiyu period from June to July 2020 by using different cloud microphysical parameterization schemes, and the simulation results of the optimal scheme were selected to explore the impact of the cloud radiative heating process on the diurnal variation characteristics of precipitation. The main conclusions are summarized as follows:

1. The simulation results of the three schemes for the precipitation distribution, regional average precipitation, and total cloud cover of the whole Meiyu period from June to July 2020 are relatively close. However, the WDM6 scheme is significantly better than the WSM3 and WSM6 schemes in simulating the heavy precipitation process. Choosing different cloud microphysical parameterization schemes has little improvement on the negative bias of afternoon precipitation peak simulation. Through statistical evaluation, it was found that the WDM6 scheme simulations were more stable and closer to the observation, with the highest time correlation coefficient for precipitation and the smallest ME and RMSE for diurnal variation.

2. In the heavy precipitation area, the WDM6 scheme perfectly reproduces the early morning peak in the diurnal variation characteristics of precipitation, but the simulation of the afternoon peak at 15:00–21:00 LST is significantly lower than the observation. This negative deviation occurs almost at the same time as the underestimation of the middle and upper clouds from afternoon to night.

3. Further analysis of the convection conditions shows that the simulation results produce cold advection transport during the dynamic convergence process at 850 hPa, resulting in abnormally low temperatures in the lower troposphere. At the same time, the underestimation of the mixing ratio of ice-phase hydrometeors in the afternoon leads to abnormal radiative heating in the middle and upper troposphere. The above two processes reduce the vertical lapse rate of atmospheric temperature and inhibit the development of thermal convection, which ultimately makes the afternoon precipitation peak seriously underestimated.

Declarations

Conflict of interest The authors declare no conflict of interest.

References

Ackerman TP, Valero FPJ, Pfister L, Lion K (1988) Heating rates in tropical anvils. J Atmos Sci 45:1606–1623. https://doi.org/10.1175/1520-0469(1988)045%3C1606:HRITA%3E2.0.CO;2

Bu W, Chen H, Li P (2022) Analysis of the deviation of forecast of ECMWF model over the Yangtze-Huaihe River Valley in summer 2020. Torrential Rain Disasters 41(3):315–323. https://doi.org/10.3969/j.issn.1004-9045.2022.03.008. (**in Chinese**)

Cai X, Zong Z, Ma J, Li Y, Zhang B, Yin S, Mei S (2020) Analysis of Meiyu characteristics and performance verification of the medium-range forecasting models in 2020. Torrential Rain Disasters 39(6):629–636. https://doi.org/10.3969/j.issn.1004-9045.2020.06.011. (**in Chinese**)

CERES_SYN1deg_Ed4A Data Quality Summary. Available online: https://ceres.larc.nasa.gov/documents/DQ_summaries/CERES_SYN1deg_Ed4A_DQS.pdf Accessed on 13 Dec 2021

Cesana G, Waliser DE, Henderson D, L'Ecuyer T, Jiang X, Li J (2019) The vertical structure of radiative heating rates: a multimodel evaluation using A-train satellite observations. J Clim 32(5):1573–1590. https://doi.org/10.1175/JCLI-D-17-0136.1

Chen G, Wang WC (2016) An effective approach to evaluate GCM simulated diurnal variation of clouds. Geophys Res Lett 43:11064–11071. https://doi.org/10.1002/2016GL070446

Chen G, Sha W, Iwasaki T, Ueno K (2012) Diurnal variation of rainfall in the Yangtze River valley during the spring-summer transition from TRMM measurements. J Geophys Res 117(D6):D06106. https://doi.org/10.1029/2011JD017056

Chen G, Sha W, Sawada M, Iwasaki T (2013) Influence of summer monsoon diurnal cycle on moisture transport and precipitation over eastern China. J Geophys Res Atmos 118(8):3163–3177. https://doi.org/10.1002/jgrd.50337

Chen T, Zhang F, Yu C, Ma J, Zhang X, Shen X, Zang F, Luo Q (2020) Synoptic analysis of extreme Meiyu precipitation over Yangtze River Basin during June-July 2020. Meteor Mon 46(11):1415–1426. https://doi.org/10.7519/j.issn.1000-0526.2020.11.003. (**in Chinese**)

Christensen MW, Carrió GG, Stephens GL, Cotton W (2013) Radiative impacts of free-tropospheric clouds on the proper-ties of marine stratocumulus. J Atmos Sci 70(10):3102–3118. https://doi.org/10.1175/JAS-D-12-0287.1

Dee DP, Uppala SM, Simmons AJ, Berrisford P, Poli P, Kobayashi S, Andrae U, Balmaseda MA, Balsamo G, Bauer P et al (2011) The ERA-Interim reanalysis: configuration and performance of the data assimilation system. QJR Meteorol Soc 137:553–597. https://doi.org/10.1002/qj.828

Ding Y, Liu J, Sun Y, Liu Y, He J, Song Y (2007) A study of the synoptic-climatology of the Meiyu system in East Asia. Chin J Atmos Sci 31(6):1082–1101. https://doi.org/10.3878/j.issn.1006-9895.2007.06.05. (**in Chinese**)

Doelling DR, Haney CO, Scarino BR, Gopalan A, Bhatt R (2016) Improvements to the geostationary visible imager ray-matching calibration algorithm for CERES edition 4. J Atmos Ocean Technol 33(12):2679–2698. https://doi.org/10.1175/JTECH-D-16-0113.1

Ge J, Wang Z, Wang C, Yang X, Dong Z, Wang M (2021) Diurnal variations of global clouds observed from the CATS spaceborne lidar and their links to large-scale meteorological factors. Clim Dyn 57:2637–2651. https://doi.org/10.1007/s00382-021-05829-2

Guan P, Chen G, Zeng W, Liu Q (2020) Corridors of Mei-Yu-season rainfall over eastern China. J Clim 33(7):2603–2626. https://doi.org/10.1175/JCLI-D-19-0649.1

Harrop BE, Hartmann DL (2016) The role of cloud radiative heating in determining the location of the ITCZ in aquaplanet simulations. J Clim 29(8):2741–2763. https://doi.org/10.1175/JCLI-D-15-0521.1

Hersbach H, Bell B, Berrisford P, Hirahara S, Horányi A, Muñoz-Sabater J, Nicolas J, Peubey C, Radu R, Schepers D et al (2020) The ERA5 global reanalysis. QJR Meteorol Soc 146:1999–2049. https://doi.org/10.1002/qj.3803

Hong S, Lim JJ (2006) The WRF single–moment 6–class microphysics scheme (WSM6). J Korean Meteor Soc 42:129–151

Hong S, Dudhia J, Chen S (2004) A revised approach to ice microphysical processes for the bulk parameterization of clouds and precipitation. Mon Weather Rev 132(1):103–120. https://doi.org/10.1175/1520-0493(2004)132%3c0103:ARATIM%3e2.0.CO;2

Hong S, Noh Y, Dudhia J (2006) A new vertical diffusion package with an explicit treatment of entrainment processes. Mon Weather Rev 134(9):2318–2341. https://doi.org/10.1175/MWR3199.1

Huang Q, Qian Y (2021) Comparative analysis of single-moment and double-moment microphysics schemes in WRF on the heavy precipitation process of the macroscale and microscale characteristic of the cloud. Trans Atmos Sci 44(04):615–625. https://doi.org/10.13878/j.cnki.dqkxxb.20190501001. (**in Chinese**)

Huang R, Cai R, Chen J, Zhou L (2006) Interdecaldal variations of drought and flooding disasters in China and their association with the east Asian climate system. Chin J Atmos Sci 30(5):730–743. https://doi.org/10.3878/j.issn.1006-9895.2006.05.02. (**in Chinese**)

Huang H, Chen C, Zhu W (2011) Impacts of different cloud microphysical processes and horizontal resolutions of WRF model on precipitation forecast effect. Meteor Sci Technol 39(05):529–536. https://doi.org/10.19517/j.1671-6345.2011.05.001. (**in Chinese**)

Iacono MJ, Delamere JS, Mlawer EJ, Shephard MW, Clough SA, Collins WD (2008) Radiative forcing by long-lived greenhouse gases: calculations with the AER radiative transfer models. J Geophys Res 113:D13103. https://doi.org/10.1029/2008JD009944

Jiang Z, Zhang D, Xia R, Qian T (2017) Diurnal variations of presummer rainfall over Southern China. J Clim 30(2):755–773. https://doi.org/10.1175/JCLI-D-15-0666.1

Jiao H, Zhao Y, Chang F, Peng X (2021) Numerical simulation of a Meiyu frontal precipitation process with the global hugh-resolution non-hydrostatic model GRAPES_YY. Meteorol Mon 47(11):1359–1368. https://doi.org/10.7519/j.issn.1000-0526.2021.11.005. (**in Chinese**)

Kain JS (2004) The Kain-Fritsch convective parameterization: an update. J Appl Meteorol Clim 43(1):170–181. https://doi.org/10.1175/1520-0450(2004)043%3c0170:TKCPAU%3e2.0.CO;2

Kato S, Rose F, Rutan D, Charlock T (2008) Cloud effects on the Meridional atmospheric energy budget estimated from clouds and the earth's radiant energy system (CERES) data. J Clim 21(17):4223–4241. https://doi.org/10.1175/2008JCLI1982.1

Kendon EJ, Roberts NM, Senior CA, Roberts MJ (2012) Realism of rainfall in a very high-resolution regional climate model. J Clim 25(17):5791–5806. https://doi.org/10.1175/JCLI-D-11-00562.1

Li J, Yu R, Zhou T (2008) Seasonal variation of the diurnal cycle of rainfall in southern contiguous China. J Clim 21(22):6036–6043. https://doi.org/10.1175/2008JCLI2188.1

Li Y, Li D, Yang S, Liu C, Zhong A, Li Y (2010) Characteristics of the precipitation over the eastern edge of the Tibetan Plateau. Meteorol Atmos Phys 106(1):49–56. https://doi.org/10.1007/s00703-009-0048-1

Lim KS, Hong S (2010) Development of an effective double-moment cloud microphysics scheme with prognostic cloud condensation nuclei (CCN) for weather and climate models. Mon Weather Rev 138(5):1587–1612. https://doi.org/10.1175/2009MWR2968.1

Lin X, Randall DA, Fowler LD (2000) Diurnal variability of the hydrologic cycle and radiative fluxes: comparisons between observations and a GCM. J Clim 13(23):4159–4159. https://doi.org/10.1175/1520-0442(2000)013%3c4159:DVOTHC%3e2.0.CO;2

Liu Y, Ding Y (2020) Characteristics and possible causes for the extreme Meiyu in 2020. Meteor Mon 46(11):1393–1404. https://doi.org/10.7519/j.issn.1000-0526.2020.11.001. (**in Chinese**)

Medeiros B, Clement AC, Benedict JJ, Zhang B (2021) Investigating the impact of cloud-radiative feedbacks on tropical precipitation extremes. Npj Clim Atmos Sci 4:18. https://doi.org/10.1038/s41612-021-00174-x

Mu X, Huang A, Wu Y, Xu Q, Zheng Y, Lin H, Fang D, Zhang X, Tang Y, Cai S (2021) Characteristics of the precipitation diurnal variation and underlying mechanisms over Jiangsu, Eastern China during warm season. Front Earth Sci 9:703071. https://doi.org/10.3389/feart.2021.703071

Niu G, Yang Z, Mitchell KE, Chen F, Ek MB, Barlage M, Kumar A, Manning K, Niyogi D, Rosero E, Tewari M, Xia Y (2011) The community Noah land surface model with multi-parameterization options (Noah–MP): 1. Model description and evaluation with local–scale measurements. J Geophys Res 116:D12109. https://doi.org/10.1029/2010JD015139

Shen Y, Hu J (2006) Slope irradiance scheme in GRAPES and its effect on simulation of short-range weather processes. Chin J Atmos Sci 30(6):1129–1137. https://doi.org/10.3878/j.issn.1006-9895.2006.06.07. (**in Chinese**)

Shen Y, Pan Y, Yu J, Zhao P, Zhou Z (2013) Quality assessment of hourly merged precipitation product over China. Trans Atmos Sci 36(1):37–46. https://doi.org/10.3969/j.issn.1674-7097.2013.01.005. (**in Chinese**)

Varga ÁJ, Breuer H (2020) Sensitivity of simulated temperature, precipitation, and global radiation to different WRF configurations over the Carpathian Basin for regional climate applications. Clim Dyn 55:2849–2866. https://doi.org/10.1007/s00382-020-05416-x

Wang F, Ding Y (2005) An Evaluation of Cloud Radiative Feedback Mechanisms in Climate Models. Adv Earth Sci 20(02):207–215. https://doi.org/10.11867/j.issn.1001-8166.2005.02.0207. (**in Chinese**)

Wang F, Yu R, Chen H, Li J, Yuan W (2011) The characteristics of rainfall diurnal variation over the Southwestern China. Torrential Rain Disasters 30(02):117–121. https://doi.org/10.3969/j.issn.1004-9045.2011.02.003. (**in Chinese**)

Wang M, Lai A, Chen Z, Bai Y, Cheng C, Li F (2012) Comparison of WRF forecast downward shortwave radiation with observations—a pilot study. Meteor Mon 38(5):585–592. https://doi.org/10.7519/j.issn.1000-0526.2012.5.009. (**in Chinese**)

Wen X, Lu S, Meng X, Wen L, Li W, Ma D (2010) Numerical simulation of oasis effect in Jinta oasis using the WRF model. Plateau Meteorol 29(5):1163–1173. https://doi.org/10.3969/j.issn.1008-6714.2016.01.012. (**in Chinese**)

Wu R, Chen G (2021) Contrasting cloud regimes and associated rainfall over the South Asian and East Asian monsoon regions. J Clim 34:3663–3681. https://doi.org/10.1175/JCLI-D-20-0992.1

Wu R, Chen G, Luo ZJ (2023) Strong coupling in diurnal variations of clouds, radiation, winds, and precipitation during the East Asian Summer Monsoon. J Clim 36(5):1347–1368. https://doi.org/10.1175/JCLI-D-22-0330.1

Xu K, Randall DA (1996) A semiempirical cloudiness parameterization for use in climate models. J Atmos Sci 53(21):3084–3102. https://doi.org/10.1175/1520-0469(1996)053%3c3084:ASCPFU%3e2.0.CO;2

Xu W, Zipser EJ (2015) Diurnal variations of precipitation, deep convection, and lightning over and east of the Eastern Tibetan Plateau. J Clim 24(2):448–465. https://doi.org/10.1175/2010JCLI3719.1

Xue M, Luo X, Zhu K, Sun Z, Fei J (2018) The controlling role of boundary layer inertial oscillations in Meiyu frontal precipitation and its diurnal cycles over China. J Geophys Res 123:5090–5115. https://doi.org/10.1029/2018JD028368

Yin J, Porporato A (2017) Diurnal cloud cycle biases in climate models. Nat Commun 8:2269. https://doi.org/10.1038/s41467-017-02369-4

Yin S, Chen D, Xie Y (2009) Diurnal variations of precipitation during the warm season over China. Int J Clim 29:1154–1170. https://doi.org/10.1002/joc.1758

Yu R, Li J (2016) Regional characteristics of diurnal peak phases of precipitation over contiguous China. Acta Meteorol Sin. https://doi.org/10.11676/qxxb2016.011. (**in Chinese**)

Yu R, Wang B, Zhou T (2004) Climate effects of the deep continental stratus clouds generated by the Tibetan Plateau. J Clim 17(13):2702–2713. https://doi.org/10.1175/1520-0442(2004)017%3c2702:CEOTDC%3e2.0.CO;2

Yu R, Xu Y, Zhou T, Li J (2007a) Relation between rainfall duration and diurnal variation in the warm season precipitation over central eastern China. Geophys Res Lett. https://doi.org/10.1029/2007GL030315

Yu R, Zhou T, Xiong A, Zhu Y, Li J (2007b) Diurnal variations of summer precipitation over contiguous China. Geophys Res Lett 34(1):223–234. https://doi.org/10.1029/2006GL028129

Yu R, Li J, Chen H, Yuan W (2014a) Progress in studies of the precipitation diurnal variation over contiguous China. J Meteorol Res 28(5):877–902. https://doi.org/10.1007/sl3351-014-3272-7

Yu R, Li J, Hao C, Yuan W (2014b) Progress in studies of the precipitation diurnal variation over contiguous China. Acta Meteorol Sin 72(5):948–968. https://doi.org/10.11676/qxxb2014.047. (**in Chinese**)

Yuan W (2013) Diurnal cycles of precipitation over subtropical China in IPCC AR5 AMIP simulations. Adv Atmos Sci 30:1679–1694. https://doi.org/10.1007/s00376-013-2250-9

Yuan W, Yu R, Zhang M, Lin W, Chen H, Li J (2012) Regimes of diurnal variation of summer rainfall over subtropical East Asia. J Clim 25(9):3307–3320. https://doi.org/10.1175/JCLI-D-11-00288.1

Zeng W, Chen G, Bai L, Liu Q, Wen Z (2022) Multiscale processes of heavy rainfall over East Asia in summer 2020: diurnal cycle in response to synoptic disturbances. Mon Weather Rev 150(6):1355–1376. https://doi.org/10.1175/MWR-D-21-0308.1

Zhang H, Xie B, Liu Y, Wang Z, Zhang J, Li J, Hu S, Shang H, Chen Y, Xuan Y (2017) Study on the influence of clouds on the earth radiation budget and precipitation changes in East Asia Region. China Basic Sci 19(05):18–22. https://doi.org/10.3969/j.issn.1009-2412.2017.05.004. (**p 28**)

Zhang A, Chen Y, Zhou S, Cui C, Wan R, Fu Y (2020a) Diurnal variation of Meiyu rainfall in the Yangtze plain during atypical Meiyu years. J Geophys Res 125(1):e2019DJ031742. https://doi.org/10.1029/2019JD031742

Zhang F, Chen T, Zhang F, Shen X, Lan Y (2020b) Extreme features of severe precipitation in Meiyu period over the middle and lower reaches of Yangtze River Basin in June–July 2020. Meteor Mon 46(11):1405–1414. https://doi.org/10.7519/j.issn.1000-0526.2020.11.003. (**in Chinese**)

Zheng X, Xu G, Wei R (2013) Introducing and influence testing of the new cloud fraction scheme in the GRAPES. Meteor Mon 39(1):57–66. https://doi.org/10.7519/j.issn.1000-0526.2013.01.007. (**in Chinese**)

Zhong Q, Sun Z, Chen H, Li J, Shen L (2022) Multi model forecast biases of the diurnal variations of intense rainfall in the Beijing–Tianjin–Hebei region. Sci China Earth Sci 65(8):1490–1509. https://doi.org/10.1007/s11430-021-9905-4

Zhou G, Zhao C, Ding S, Qin Y (2005) A study on impacts of different radiative transfer schemes on mesoscale precipitations. J Appl Meteorol Sci 16(02):148–158. https://doi.org/10.11898/1001-7313.20050203. (**in Chinese**)

Zhou T, Yu R, Chen H, Dai A, Pan Y (2008) Summer precipitation frequency, intensity, and diurnal cycle over china: a comparison of satellite data with rain gauge observations. J Clim 21(16):3997–4010. https://doi.org/10.1175/2008JCLI2028.1

Zhou Z, Deng Y, Hu Y, Kang Z (2020) Simulating heavy Meiyu rainfall: a note on the choice of the model microphysics scheme. Adv Meteorol. https://doi.org/10.1155/2020/8827071